

NLO QCD corrections to the electroweak production of a Higgs boson pair in the quark-antiquark channel

Marco Bonetti,^{a,b,c} Gudrun Heinrich,^b Philipp Rendler,^b William J. Torres Bobadilla^d

^a*Institute for Theoretical Physics, University of Tübingen, Auf der Morgenstelle 14, 72076 Tübingen, Germany*

^b*Institute for Theoretical Physics, Karlsruhe Institute of Technology (KIT), Wolfgang-Gaede-Str. 1, 76131 Karlsruhe, Germany*

^c*Institute for Astroparticle Physics, Karlsruhe Institute of Technology (KIT), 76344 Eggenstein-Leopoldshafen, Germany*

^d*Department of Mathematical Sciences, University of Liverpool, Liverpool L69 3BX, U.K.*

E-mail: marco.bonetti@uni-tuebingen.de, gudrun.heinrich@kit.edu,
philipp.rendler@kit.edu, torres@liverpool.ac.uk

ABSTRACT: Higgs boson pair production in the massless quark-antiquark channel proceeds at leading order (LO) via electroweak boson loops. We calculate the next-to-leading order QCD corrections to this process. For the corresponding two-loop amplitudes, an analytic representation has been achieved. Even though the size of this contribution at the level of total cross sections is below 1% compared to the LO gluon channel, the effect on differential observables can be in the 10% range and therefore this contribution should be taken into account when comparing to LHC data.

KEYWORDS: LHC, Higgs boson, electroweak corrections

Contents

1	Introduction	1
2	Scattering amplitudes	3
2.1	General structure	3
2.2	LO & virtual NLO amplitudes	6
2.3	Real NLO amplitudes	7
3	Master Integrals	8
3.1	Mathematical framework	8
3.2	Amplitude evaluation	9
4	Phenomenological results	10
4.1	Differential distributions	11
4.2	Bottom quark effects	12
5	Conclusions	13
A	Canonical DEQ for $\mathcal{A}^{(1)}$	14

1 Introduction

Higgs boson pair production is an important process at the LHC because it is the only direct way to measure the trilinear Higgs self-coupling and thus experimentally probe the shape of the Higgs potential and electroweak symmetry breaking. Projections for the High-Luminosity LHC reach an accuracy level on the trilinear Higgs coupling of about 30% [1] after collecting an integrated luminosity of 3 ab^{-1} . However, this scenario relies on the assumption that the theory uncertainties will be halved by then. Therefore, theoretical predictions for Higgs boson pair production, in particular for the gluon fusion mode that has the largest cross section, need to reach a level of precision where electroweak corrections cannot be neglected.

Higgs boson pair production in gluon fusion is mediated by heavy quark loops at leading order (LO), calculated for the first time in Refs. [2, 3]. As the next-to-leading order (NLO) corrections involve two-loop integrals with several mass scales, the NLO QCD corrections were first calculated in the heavy-top-limit (HTL), rescaled with the top-mass dependent LO amplitude [4]. The NLO QCD corrections including the full top-quark mass dependence became available later [5–9], increasing the total LO cross section by about 60%. The full NLO QCD corrections of Refs. [5, 6] have been combined with a calculation at approximate NNLO, where the top mass dependence is also included in the real radiation matrix element [10], called NNLO_{FTapprox}. Earlier work has provided NNLO results

in the HTL improved by an expansion by powers in $1/m_t^2$ [11, 12]. Matching of the NLO corrections to parton showers has been performed in Refs. [13–17] in the POWHEG-BOX-V2 framework, recently also including corrections at approximate NNLO in the GENEVA framework [18]. N^3LO corrections [19, 20] and N^3LO+N^3LL corrections [21] in the heavy-top-limit are also known. The N^3LO results have a residual scale uncertainty of about 3%. This means that other uncertainties, such as top mass renormalisation scheme uncertainties or electroweak (EW) corrections gain increasing relevance in the uncertainty budget. Currently, the top-mass renormalisation scheme uncertainties are the largest uncertainties for this process [16, 22], they are estimated to be of the order of 20%. However, the large logarithms responsible for the differences between \overline{MS} and on-shell schemes for the top-quark mass at high energies have been identified [23]. Furthermore, partial three-loop results have been obtained recently [24–27], where in Ref. [26] it is shown that the mass scheme dependence is reduced significantly at this order.

With these prospects the contributions to Higgs boson pair production of EW type are a source of uncertainty which urgently needs to be reduced, in particular as it is known that EW corrections can significantly affect the shapes of observables. First partial NLO EW corrections to Higgs boson pair production have been calculated in Refs. [28–30]. The possibility to constrain the quartic Higgs boson coupling indirectly through (partial) EW corrections to Higgs boson pair production has been explored in Refs. [28, 31, 32]. The Yukawa and Higgs boson self-coupling corrections have been calculated in Ref. [33] using a numerical approach, and in Ref. [34] based on a high-energy expansion. The EW corrections involving light quarks have been calculated analytically in Ref. [35]. Top-Yukawa- and light-quark-mediated EW corrections have been presented in Ref. [36]. The NLO EW corrections in the large top-quark mass expansion up to $1/m_t^8$ have been calculated in Ref. [37], the NLO EW corrections with full m_t -dependence have been calculated in Ref. [38], finding that the NLO EW corrections decrease the total cross section by about 4% and distort the Higgs boson pair invariant mass (m_{HH}) distribution close to the Higgs pair production threshold and at high energies.

In this work, we present the calculation of the mixed QCD-EW contributions to Higgs boson pair production, where at LO the Higgs bosons are produced by light quarks in the initial state through couplings to electroweak bosons, while the QCD corrections involve real and virtual gluons. Due to the large gluon luminosity at the LHC, this contribution is not expected to be large. However, we will show that the effects close to the Higgs pair production threshold on the shape of the Higgs boson pair invariant mass distribution are relatively large. As this is a kinematic region that is very sensitive to deviations of the trilinear coupling from its SM value, it is important to include all SM contributions that may affect the low- m_{HH} region at percent level. The corresponding code will be made publicly available within the POWHEG-BOX-V2 [39] framework.

This paper is organised as follows. In Section 2, we describe the structure of the amplitudes and the setup of our calculation. Section 3 is dedicated to the analytic calculation of the one- and two-loop form factors. In Section 4 we present phenomenological results, both at total cross section level and for differential observables, before we conclude in Section 5.

2 Scattering amplitudes

2.1 General structure

We consider the production of two Higgs bosons from a quark and an antiquark, where the Higgs bosons couple to vector bosons, see Table 1 for representative diagrams. At LO, this is an electroweak process and we calculate NLO QCD corrections to it. We use the “all incoming” convention to label the momenta, therefore we have

$$\bar{q}(p_1) q(p_2) \rightarrow H(-p_3) H(-p_4) \quad (2.1)$$

for the LO and the NLO virtual contributions, and we use p_5 for the additional gluon momentum present in the real radiation diagrams. We use four incoming light flavours, $q \in \{u, d, s, c\}$, with $p_1^2 = p_2^2 = 0$, and consider the Higgs bosons and the gluon to be on-shell ($p_3^2 = p_4^2 = m_H^2$, $p_5^2 = 0$).

As we only consider massless quarks, no Yukawa couplings to the Higgs boson are present. As a consequence, the Higgs bosons can only be generated through vertices with two electroweak (or Goldstone) bosons, resulting in the LO being already a loop-mediated contribution. We neglect bottom quarks in the initial state, as they are suppressed by the parton distribution functions (PDFs) relative to the lighter quarks. Assuming a diagonal CKM matrix, this implies that no top quarks are contained in the two-loop diagrams. We discuss the impact of bottom quark contributions in Sec. 4.

All diagrams considered here can be classified according to the production mode of the Higgs boson pair, see Table 1 and Ref. [35].¹

We start by considering *bridge diagrams*, where a gauge boson line acts a bridge connecting two 1PI parts of a diagram. These diagrams are zero either by colour (when a gluon acts as a bridge) or by angular momentum conservation (when a photon or a Z boson connects the two parts of the diagram).

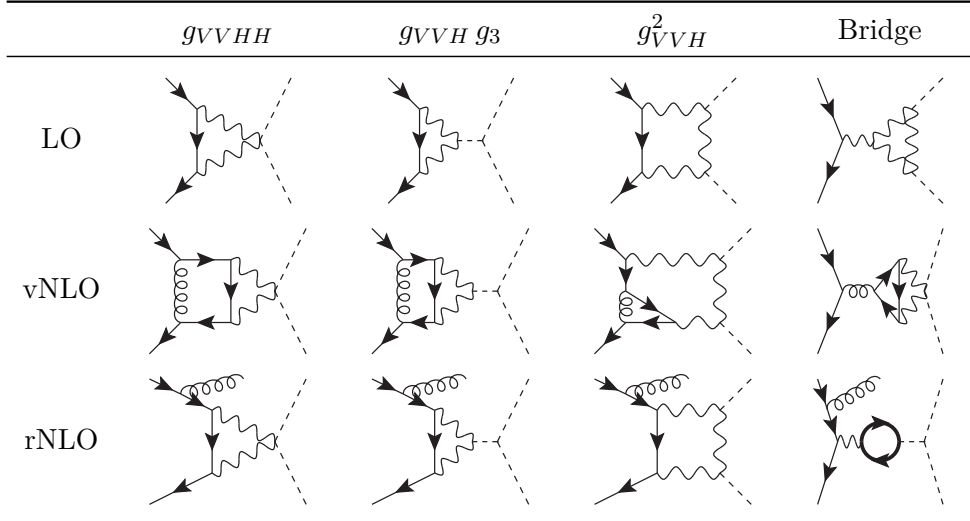
The remaining diagrams can be classified into three categories: diagrams proportional to g_{VVH} , containing a four-point vertex connecting two EW bosons and two Higgs bosons, diagrams proportional to $g_{VVH} g_3$, where two EW bosons merge into an s -channel Higgs boson subsequently splitting into two, thus containing the trilinear Higgs coupling g_3 , and diagrams proportional to g_{VVH}^2 , where each Higgs boson is produced from a different VVH three-point vertex. In all these cases, each individual diagram contains either W or Z bosons only (plus the corresponding Goldstone bosons). Each of these three categories is gauge-invariant and closed under renormalisation and IR subtraction.²

Due to angular momentum conservation, the diagrams proportional to g_{VVH} and $g_{VVH} g_3$ are zero for LO and virtual NLO contributions, leaving only diagrams of g_{VVH}^2 -type to contribute at LO and at two-loop order.

¹We adopt here a slightly different notation w.r.t. [35], oriented at the coupling structures rather than the propagators. For comparison, g_{VVH} here corresponds to $VVHH$ of [35], $g_{VVH} g_3$ to VVH , and g_{VVH}^2 to VVV .

²We explicitly computed diagrams in both unitary and Feynman gauge, finding identical expressions for each category.

Table 1: Example diagrams for different classes of contributions to $q\bar{q} \rightarrow HH (+g)$ at LO, virtual NLO, and real NLO. Each class features diagrams containing either only W (Goldstone) bosons, or only Z (Goldstone) bosons.



W and Z bosons interact with quarks through vertices of the form $\gamma^\mu(g_L \mathbb{P}_L + g_R \mathbb{P}_R)$, potentially introducing traces of gamma matrices containing γ_5 and resulting in Levi-Civita symbols. We avoid this by considering polarised states for the external quarks, according to the following procedure.

Up to two loops, W and Z bosons are always attached to the same open fermion line, therefore we can anticommute all $\mathbb{P}_{L,R}$ projectors until they touch the rightmost spinor (u_2) in the $\bar{u}_1 \gamma \cdots \gamma u_2$ chain.³ The result is equivalent to selecting a specific polarisation of the external states, starting from a theory where W and Z bosons couple only vectorially to the fermions, later characterising specific polarisation configurations by different couplings. Accordingly, we treat the amplitude as free from γ_5 terms and reinstate them only at the very end, when considering different helicity configurations.

A potential risk in this procedure is that some of the diagrams might require an even number of anticommutations to move the $\mathbb{P}_{L,R}$ projectors to the rightmost end of the spinor chain, while some other an odd number. As a result, some diagrams with the axial terms stripped off might be equal to *minus* the corresponding diagram with vector couplings only, while some others to *plus* the corresponding diagram, not allowing us to calculate the amplitude as a whole starting from vector-only couplings and then extract the single helicity amplitudes. However, this is not the case: we are considering massless quarks and QCD corrections, therefore the $q\bar{q}V$ vertex closest to u_2 can either be already attached to it or have n $q\bar{q}g$ vertices and massless quark propagators in between, requiring in both cases $2n$ anticommutations to bring the $\mathbb{P}_{L,R}$ next to u_2 , therefore producing no relative minus sign for any of the diagrams.

³Since we are working in dimensional regularisation, γ_5 is not properly defined, and requires a scheme choice to be consistently handled. We rely on the Kreimer scheme [40, 41].

As a consequence, the sum of the resulting ‘‘vector-type’’ diagrams remains consistent with the sum of the original diagrams.

We can now write the $q\bar{q} \rightarrow HH$ and $q\bar{q} \rightarrow HHg$ amplitudes, respectively, as

$$\begin{aligned} M_{i_1 i_2}^{s_1 s_2, q_1 q_2} &= \delta_{i_1 i_2} \sum_{V=W,Z} \bar{u}_{q_1}^{s_1}(p_1) \tilde{\mathcal{M}}(m_V^2) [G_{V,L}^{q_1 q_2} \mathbb{P}_L + G_{V,R}^{q_1 q_2} \mathbb{P}_R] u_{q_2}^{s_2}(p_2), \\ M_{c,i_1 i_2}^{s_1 s_2 \lambda, q_1 q_2} &= (T_c)_{i_1 i_2} \sum_{V=W,Z} \bar{u}_{q_1}^{s_1}(p_1) \tilde{\mathcal{M}}^\mu(m_V^2) [G_{V,L}^{q_1 q_2} \mathbb{P}_L + G_{V,R}^{q_1 q_2} \mathbb{P}_R] u_{q_2}^{s_2}(p_2) \epsilon_\mu^{*\lambda}(p_5), \end{aligned} \quad (2.2)$$

with abuse of notation in the momentum conservation, $p_1 + \dots + p_4 (+p_5) = 0$; i_1 and i_2 are the antiquark and quark colour indices, respectively, s_1 and s_2 the spin indices, q_1 and q_2 the flavour indices, c the colour index of the extra gluon, λ its polarisation, and $\tilde{\mathcal{M}}$ and $\tilde{\mathcal{M}}^\mu$ the amplitudes where each $q\bar{q}V$ vertex has been replaced with a pure vector interaction, which can be further decomposed, following to Table 1, into

$$\tilde{\mathcal{M}} = \tilde{\mathcal{M}}_{g_{WWH}^2} + \tilde{\mathcal{M}}_{g_{ZZH}^2} \quad (2.3)$$

and

$$\tilde{\mathcal{M}}^\mu = \tilde{\mathcal{M}}_{g_{WWHH}^{\mu}} + \tilde{\mathcal{M}}_{g_{WWHg_3}^{\mu}} + \tilde{\mathcal{M}}_{g_{WWH}^2}^\mu + \tilde{\mathcal{M}}_{g_{ZZHH}^{\mu}} + \tilde{\mathcal{M}}_{g_{ZZHg_3}^{\mu}} + \tilde{\mathcal{M}}_{g_{ZZH}^2}^\mu. \quad (2.4)$$

The $G_{V,L/R}^{q_1 q_2}$ couplings encapsulate the SM EW coupling structure of the different parts of the amplitude and read (cf. [42–44])

$$G_{W,L}^{q_1 q_2} = \begin{cases} \sum_{k \in \{d,s\}} \mathcal{V}_{q_1 k}^* \mathcal{V}_{k q_2} & \text{if } q_1 \in \{u,c\} \\ \sum_{k \in \{u,c\}} \mathcal{V}_{k q_1} \mathcal{V}_{q_2 k}^* & \text{if } q_1 \in \{d,s\} \end{cases} \quad (2.5)$$

$$G_{W,R}^{q_1 q_2} = 0 \quad (2.6)$$

$$G_{Z,L}^{q_1 q_2} = \frac{2\delta_{q_1 q_2}}{c_W^4} (g_L^{q_1 q_2})^2 = \begin{cases} \frac{1}{c_W^4} \left(\frac{1}{2} - \frac{4}{3} s_W^2 + \frac{8}{9} s_W^4 \right) & \text{if } q_1 = q_2 \in \{u,c\} \\ \frac{1}{c_W^4} \left(\frac{1}{2} - \frac{2}{3} s_W^2 + \frac{2}{9} s_W^4 \right) & \text{if } q_1 = q_2 \in \{d,s\} \end{cases} \quad (2.7)$$

$$G_{Z,R}^{q_1 q_2} = \frac{2\delta_{q_1 q_2}}{c_W^4} (g_R^{q_1 q_2})^2 = \begin{cases} \frac{1}{c_W^4} \left(\frac{8}{9} s_W^4 \right) & \text{if } q_1 = q_2 \in \{u,c\} \\ \frac{1}{c_W^4} \left(\frac{2}{9} s_W^4 \right) & \text{if } q_1 = q_2 \in \{d,s\} \end{cases} \quad (2.8)$$

(\mathcal{V} is the Cabibbo–Kobayashi–Maskawa mixing matrix, $c_W = \cos \theta_W$, $s_W = \sin \theta_W$, and θ_W is the Weinberg angle).

In terms of helicity amplitudes, we have only two non-zero configurations for the $q\bar{q} \rightarrow HH$ case:

$$M_{i_1 i_2}^{-+, q_1 q_2} = \delta_{i_1 i_2} \sum_{V=W,Z} G_{V,R}^{q_1 q_2} [1| \tilde{\mathcal{M}}(m_V^2) |2], \quad (2.9)$$

$$M_{i_1 i_2}^{+-, q_1 q_2} = \delta_{i_1 i_2} \sum_{V=W,Z} G_{V,L}^{q_1 q_2} \langle 1 | \tilde{\mathcal{M}}(m_V^2) | 2 \rangle. \quad (2.10)$$

Notice that the two configurations, up to $G_{V,L/R}^{q_1 q_2}$ coefficients, are related by complex conjugation of the spinor structures, resulting in only one independent non-zero helicity expression. This is consistent with working with a purely vectorial amplitude, reconstructing the axial contributions at a later stage.

For $q\bar{q} \rightarrow HHg$ we obtain four non-zero configurations:

$$M_{i_1 i_2}^{---, q_1 q_2} = (T_c)_{i_1 i_2} \sum_{V=W,Z} \delta_{i_1 i_2} G_{V,R}^{q_1 q_2} [1 | \tilde{\mathcal{M}}^\mu(m_V^2) | 2 \rangle \frac{[r | \gamma_\mu | 5 \rangle}{\sqrt{2}[5r]}, \quad (2.11)$$

$$M_{i_1 i_2}^{+-+, q_1 q_2} = (T_c)_{i_1 i_2} \sum_{V=W,Z} \delta_{i_1 i_2} G_{V,L}^{q_1 q_2} \langle 1 | \tilde{\mathcal{M}}^\mu(m_V^2) | 2 \rangle \frac{[r | \gamma_\mu | 5 \rangle}{\sqrt{2}[5r]}; \quad (2.12)$$

$$M_{c,i_1 i_2}^{--+ , q_1 q_2} = (T_c)_{i_1 i_2} \sum_{V=W,Z} \delta_{i_1 i_2} G_{V,R}^{q_1 q_2} [1 | \tilde{\mathcal{M}}^\mu(m_V^2) | 2 \rangle \frac{\langle r | \gamma_\mu | 5 \rangle}{\sqrt{2}\langle r 5 \rangle}, \quad (2.13)$$

$$M_{c,i_1 i_2}^{+-- , q_1 q_2} = (T_c)_{i_1 i_2} \sum_{V=W,Z} \delta_{i_1 i_2} G_{V,L}^{q_1 q_2} \langle 1 | \tilde{\mathcal{M}}^\mu(m_V^2) | 2 \rangle \frac{\langle r | \gamma_\mu | 5 \rangle}{\sqrt{2}\langle r 5 \rangle}, \quad (2.14)$$

where r is the reference vector associated to the gluon polarization. Here as well, up to the electroweak prefactors $G_{V,L/R}^{q_1 q_2}$, the $+-+$ and $-+-$ as well as the $-++$ and $++-$ helicity configurations are related by complex conjugation of the spinor structures.

2.2 LO & virtual NLO amplitudes

Once stripped from its axial contributions, the $q\bar{q} \rightarrow HH$ amplitude can be written in terms of a single form factor as

$$\bar{u}^{s_1}(p_1) \tilde{\mathcal{M}}_{g_{VH}^2}(m_V^2) u^{s_2}(p_2) = \bar{u}^{s_1}(p_1) \not{p}_3 u^{s_2}(p_2) \mathcal{F}_{g_{VH}^2}(m_V^2), \quad (2.15)$$

with $V = W, Z$.⁴ The bare form factor $\mathcal{F}_{g_{VH}^2}(m_V^2)$ admits the decomposition

$$\mathcal{F}_{g_{VH}^2}(m_V^2) = g_{VH}^2 \omega_q(m_V^2) \sum_{L=1}^{\infty} a^{L-1}(m_V^2) \mathcal{A}^{(L)}(m_V^2), \quad (2.16)$$

with $g_{VH} = 1$ in the SM and

$$\omega_q(m_V^2) = i(4\pi)^\epsilon e^{-\gamma_E \epsilon} \left(\frac{m_V^2}{\mu_{\text{EW}}^2} \right)^{-\epsilon} \frac{\alpha^2}{m_V^2 \sin^4 \theta_W}, \quad (2.17)$$

$$a(m_V^2) = (4\pi)^\epsilon e^{-\gamma_E \epsilon} \left(\frac{m_V^2}{\mu^2} \right)^{-\epsilon} \left(\frac{\alpha_S}{2\pi} \right), \quad (2.18)$$

where μ_{EW}^2 and μ^2 are the regularisation parameters coming from loop integrals—the first one from the LO EW couplings, the second one from higher-order QCD corrections. We

⁴This is again consistent with the existence of a single independent non-zero helicity configuration, see [45, 46].

define the Mandelstam invariants as

$$\begin{aligned} s &= (p_1 + p_2)^2, \\ t &= (p_1 + p_3)^2, \\ u &= (p_2 + p_3)^2, \end{aligned} \tag{2.19}$$

obeying $s + t + u = 2m_H^2$, with momenta defined as in Eq. (2.1).

The form factor $\mathcal{F}_{g_{VVH}^2}(m_V^2)$ can be extracted by applying the projector

$$\mathbb{P}^{s_2 s_1} = -\frac{\bar{u}^{s_2}(p_2) \not{p}_3 u^{s_1}(p_1)}{2(m_H^4 - tu)} \tag{2.20}$$

to the amplitude as

$$\mathcal{F}_{g_{VVH}^2}(m_V^2) = \bar{u}^{s_1}(p_1) \tilde{\mathcal{M}}_{g_{VVH}^2}(m_V^2) u^{s_2}(p_2) \mathbb{P}^{s_2 s_1}. \tag{2.21}$$

We extract the virtual NLO finite remainder following the procedure described in [47]. We first employ the $\overline{\text{MS}}$ renormalisation scheme for the strong coupling

$$\alpha_S = \frac{1}{S_\epsilon} \left(\frac{\bar{\mu}^2}{\mu^2} \right)^\epsilon \overline{\alpha_S}(\bar{\mu}^2) [1 + \mathcal{O}(\overline{\alpha_S})], \tag{2.22}$$

where α_S is the bare coupling, $\overline{\alpha_S}(\bar{\mu}^2)$ is the renormalised one, $\bar{\mu}^2$ is the renormalisation scale, and $S_\epsilon = e^{-\gamma_E \epsilon} (4\pi)^\epsilon$. We then apply the operator

$$\mathbf{I}_1 = -C_F \left(\frac{2}{\epsilon^2} + \frac{3}{\epsilon} \right) \frac{e^{\gamma_E \epsilon}}{2\Gamma(1-\epsilon)} \left(-\frac{\bar{\mu}^2}{s} \right)^\epsilon, \tag{2.23}$$

with $C_F = (N_C^2 - 1)/(2N_C)$, to extract the finite remainder as

$$\mathcal{A}_{\text{fin}}^{(2)} = \mathcal{A}^{(2)} - \left(\frac{m_V^2}{\bar{\mu}^2} \right)^\epsilon \mathcal{A}^{(1)} \mathbf{I}_1. \tag{2.24}$$

2.3 Real NLO amplitudes

Real corrections are provided by the process $q\bar{q} \rightarrow HHg$, together with its permutations $qg \rightarrow HHq$ and $\bar{q}g \rightarrow HH\bar{q}$, where the configuration $g_{VVHH} = g_{VVH} = g_3 = 1$ corresponds to the SM. Contrary to what was observed for LO and virtual corrections, contributions proportional to g_{VVHH} and $g_{VVH} g_3$ are non-zero here, thanks to the angular momentum carried by the extra gluon.

While the g_{VVH}^2 contributions will present standard NLO soft and collinear divergences due to the extra gluon, the novel g_{VVHH} and $g_{VVH} g_3$ contributions are finite in the same phase-space regions, due to the corresponding LO contributions being zero. This can be seen already at the diagram level in the soft limit by employing the soft Feynman rules presented in [48] and in the collinear limit performing a similar analysis.

We automatically generate the real emission contributions using the computer code GoSAM [49–51].

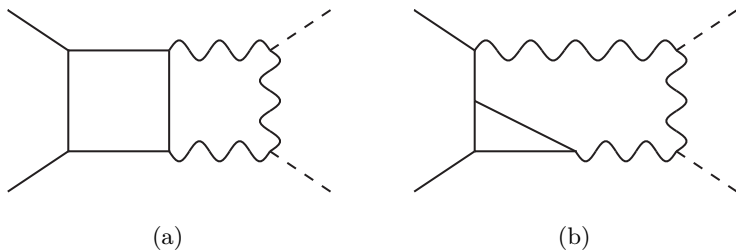


Figure 1: Two-loop top sectors. Massless particles are indicated by straight lines, particles with mass m_V by wavy lines, and particles with mass m_H by dashed lines.

3 Master Integrals

3.1 Mathematical framework

For the analytic evaluation of the form factors at one and two loops, we adopt the standard methodology used for multi-loop scattering amplitudes. We begin by reducing the relevant Feynman integrals to a minimal set of master integrals using integration-by-parts (IBP) identities [52, 53], implemented through REDUCE [54, 55] and KIRA [56–59]. We then construct a basis of master integrals that satisfy a canonical system of differential equations [60] using LITERED [61] and FINITEFLOW [62]. At one loop, we identify 11 canonical master integrals, determined by analysing their leading and Landau singularities, along the lines of [63]. At two loops, only planar integrals are required for the computation of the form factor $\mathcal{A}^{(2)}$, specifically those illustrated in Fig. 1. All master integrals associated with the double-box topology shown in Fig. 1a were recently computed in [35]. To complete the canonical basis, only six additional integrals—derived from the topology in Fig. 1b—are needed. We identify the missing integrals with the help of DLOGBASIS [64]. Let us remark that the integration kernels in the canonical differential equations (or letters of the kinematic alphabet) are contained in the alphabet reported in [35]. Hence, no new letters arise from the topology in Fig. 1b.

Once the complete set of master integrals is established, we rotate the integral basis to a basis of graded transcendental functions, as described in [65, 66]. This functional organisation not only simplifies the analytic structure of the result but also ensures efficient cancellation of IR poles when computing the finite remainder at two loops. In particular, we incorporate the Catani subtraction operator (2.23) to handle the IR structure of the one-loop amplitude, and we ensure that the transcendental functions are organised in a way that allows for a matching of transcendental functions of the leading and subleading ϵ poles at two loops. This is achieved by identifying relations between products of logarithms and the independent transcendental functions. For the remaining integrals, boundary constants are calculated in the limit $s, t, u \ll m_V^2$, often referred to as the large-mass expansion, in the same way as carried out in [35].

For the sake of reproducibility and to facilitate further analysis, we provide supplemental material at [67] with the full expressions for the one- and two-loop bare amplitudes

$\mathcal{A}^{(1)}$ and $\mathcal{A}^{(2)}$, expanded up to $\mathcal{O}(\epsilon^2)$ and $\mathcal{O}(\epsilon^0)$, respectively, as well as the finite remainder $\mathcal{A}_{\text{fin}}^{(2)}$. These expressions are given in terms of our chosen basis of independent transcendental functions together with their explicit representation as Chen iterated integrals.

3.2 Amplitude evaluation

We follow the same strategy as outlined in [35] to provide numerical values, starting either from our basis of independent transcendental functions or from the single Chen iterated integrals. Namely, we evolve the boundary point to the desired target point by solving the differential equations numerically with the help of DIFFEXP [68, 69]. Our expressions can also be interfaced with other codes which support complex kinematics [70–72].

We begin by studying the analytic structure of the one-loop form factor, $\mathcal{A}^{(1)}$, expressed in terms of independent transcendental functions, say $w^{(k)}$, with k the transcendental weight. This allows us to make manifest the functional relations and simplifications that emerge in the finite remainder, and provides insight into the interplay between the algebraic and transcendental structures of the amplitude. The finite contribution to the one-loop form factor $\mathcal{A}^{(1)}$ simply becomes:

$$\begin{aligned} \mathcal{A}_{\text{fin}}^{(1)} = & \frac{(t-u)(t+u-4)}{4r_1(m_H^4-tu)}w_{72}^{(2)} + \frac{(u-t)}{4(m_H^4-tu)}w_{132}^{(2)} + \frac{(t-2)}{2(m_H^4-tu)}w_{22}^{(2)} - \frac{(u-2)}{2(m_H^4-tu)}w_{202}^{(2)} \\ & + \frac{1}{2r_3} \left(1-t + \frac{(t-2)((s-1)t+u)}{2(m_H^4-tu)} \right) w_{102}^{(2)} \\ & - \frac{1}{2r_8} \left(1-u + \frac{(u-2)((s-1)u+t)}{2(m_H^4-tu)} \right) w_{232}^{(2)}. \end{aligned} \quad (3.1)$$

where we set $m_V = 1$, and the transcendental functions $w^{(2)}$ obey the system of differential equations, following the strategy of [73],

$$d\vec{\omega}_{1;0} = d\Omega_{1;0} \vec{\omega}_{1;0}, \quad (3.2)$$

with,

$$\vec{w}_{3:0} = \{w_{10}^{(0)}, w_{11}^{(1)}, w_{21}^{(1)}, w_{51}^{(1)}, w_{71}^{(1)}, w_{22}^{(2)}, w_{72}^{(2)}, w_{102}^{(2)}, w_{132}^{(2)}, w_{202}^{(2)}, w_{232}^{(2)}\}, \quad (3.3)$$

and the only non-vanishing boundary value at $s = 0$,

$$w_{10}^{(0)}|_{s=0} = -1, \quad (3.4)$$

In Appendix A, we provide the explicit form of the differential equations satisfied by the functions appearing in Eq. (3.1), along with precise definitions of the square roots r_1, r_3, r_8 that enter the alphabet of the system. For a more detailed discussion of the underlying method, we refer the reader to [35].

Since the one- and two-loop canonical integrals are both expressed in terms of the same set of transcendental functions, we construct a unified system of 152 differential equations for all functions appearing in $\mathcal{A}^{(1)}$ and $\mathcal{A}^{(2)}$. Although these form factors depend

Table 2: Real and imaginary parts of the numerical evaluation of the LO ($\mathcal{A}^{(1)}$), bare virtual NLO ($\mathcal{A}^{(2)}$), and NLO finite remainder ($\mathcal{A}_{\text{fin}}^{(2)}$) amplitudes at the phase-space point of Eq. (3.5).

$\mathcal{A}^{(1)}, \epsilon^0$	0.11720874553989	—	0.11116963414362 i
$\mathcal{A}^{(1)}, \epsilon^1$	0.06744433484893	+	0.15073003495756 i
$\mathcal{A}^{(1)}, \epsilon^2$	-0.100790286461074	+	0.013669915468337 i
$\mathcal{A}^{(2)}, \epsilon^{-2}$	-0.156278327386515	+	0.148226178858166 i
$\mathcal{A}^{(2)}, \epsilon^{-1}$	-0.290675394584724	—	0.943203210511806 i
$\mathcal{A}^{(2)}, \epsilon^0$	1.666836281405315	+	0.560490323962583 i
$\mathcal{A}_{\text{fin}}^{(2)}$	-0.891755853165636	+	0.495448608356593 i

on a smaller subset—92 independent transcendental functions—additional equations are required to close the system of differential equations. These differential equations are organised according to their transcendental weight, which reflects the number of iterated integrations.

We numerically evaluate the one- and two-loop form factors at the following phase-space point in the physical region

$$\{s_0, t_0, u_0, m_{V;0}^2\} = \left\{ \frac{3125}{128}, -\frac{1875}{128}, -\frac{625}{128}, 1 \right\}. \quad (3.5)$$

In Table 2, we present the numerical values of the ϵ expansions for the form factors $\mathcal{A}^{(1)}$ and $\mathcal{A}^{(2)}$, as well as the two-loop finite remainder $\mathcal{A}_{\text{fin}}^{(2)}$.

To validate our implementation, we compare the numerical evaluation of the canonical integrals appearing in the form factors with results obtained using AMFLOW [74, 75], finding agreement up to about 20 digits.

4 Phenomenological results

We combine the LO and NLO (real and virtual) amplitudes using the POWHEG-Box-V2 framework [39, 76, 77] combined with GoSAM-3.0 [51]. We calculate the total cross sections at proton-proton centre-of-mass energies of $\sqrt{S} = 13$ TeV, $\sqrt{S} = 13.6$ TeV and $\sqrt{S} = 14$ TeV, using the PDF4LHC21_40 parton distribution function (PDF) set [78]. For our differential results we use $\sqrt{S} = 13.6$ TeV. As electroweak input parameters we choose the gauge boson masses $m_W = 80.36$ GeV, $m_Z = 91.1876$ GeV, together with the Fermi constant $G_F = 0.116639 \times 10^{-4}$ GeV $^{-2}$. The mass of the Higgs boson is fixed to 125.0 GeV, and the widths of the gauge bosons are neglected. The renormalisation and factorisation scales are dynamically chosen to $\mu_F = \bar{\mu} = m_{HH}/2$. Scale uncertainties for the quark-antiquark channel are determined using a 7-point variation, varying $\bar{\mu}$ and μ_F independently by factors of 1/2 and 2, while omitting the combinations $(\bar{\mu}, \mu_F) = (m_{HH}/4, m_{HH})$ and $(m_{HH}, m_{HH}/4)$.

Table 3: Total LO and NLO cross sections at proton-proton centre-of-mass energies of 13.0 TeV, 13.6 TeV and 14.0 TeV.

\sqrt{S} [TeV]	$q\bar{q}_{\text{LO}}$ [fb]	$q\bar{q}_{\text{NLO}}$ [fb]	gg_{LO} [fb]	$q\bar{q}_{\text{NLO}}/q\bar{q}_{\text{LO}}$	$q\bar{q}_{\text{NLO}}/gg_{\text{LO}}$
13.0	0.039	0.061	16.45	+59%	+0.37%
13.6	0.041	0.066	18.26	+60%	+0.36%
14.0	0.043	0.069	19.52	+60%	+0.35%

In Table 3, we report the total cross sections for the quark-antiquark channel at LO and NLO as well as the LO contribution from the gluon channel. The large K-factor between LO and NLO can be understood from the fact that the gluon radiation opens up new partonic channels, such as qg , which are less suppressed by the PDFs than the $q\bar{q}$ channel.

4.1 Differential distributions

We provide differential distributions for the invariant mass of the Higgs boson pair, m_{HH} , the transverse momentum of one Higgs boson, p_T , and the rapidity y of one Higgs boson, shown in Figure 2 (top left, top right, and bottom, respectively). For comparison, the LO (blue) and NLO (orange) contributions from the quark-antiquark channel are shown on top of the LO gluon-fusion contribution (green). The upper subplots show the absolute values, while the lower subplots show the relative effect with respect to the gluon channel.

For the invariant mass distribution (top left), we observe an enhancement of nearly +10% in the leftmost bin, which is largely driven by real emission contributions and is almost absent at LO. In this kinematic region, two enhancement mechanisms combine:

1. The real emission amplitude is enhanced for m_{HH} values close to the production threshold, corresponding to configurations where a hard jet recoils against the Higgs boson pair.
2. The real emission contribution includes initial-state gluon splittings into quark-antiquark pairs, which enhance the differential cross section due to the dominance of gluon PDFs at the LHC.

In addition, the quark-antiquark channel produces an enhancement in the high- m_{HH} tail of the distribution, where logarithms of Sudakov-type, $\log(\hat{s}/m_V^2)$, grow large.

For the real radiation diagrams, we observe destructive interference between triangle-type and box-type diagrams (cf. the last line in Table 1), similar to the gluon fusion case, while for the virtual corrections this behaviour is absent since the triangle-type diagrams vanish. Therefore we anticipate a large sensitivity to modifications of the Higgs couplings (changing the interference pattern) from the real radiation contributions.

The transverse momentum distribution (top right) of one of the Higgs bosons exhibits a pattern similar to that observed in the invariant-mass distribution: An enhancement at low p_T , primarily driven by real emission contributions, as well as an increase in the high- p_T tail, still modest at p_T values of about 700 GeV.

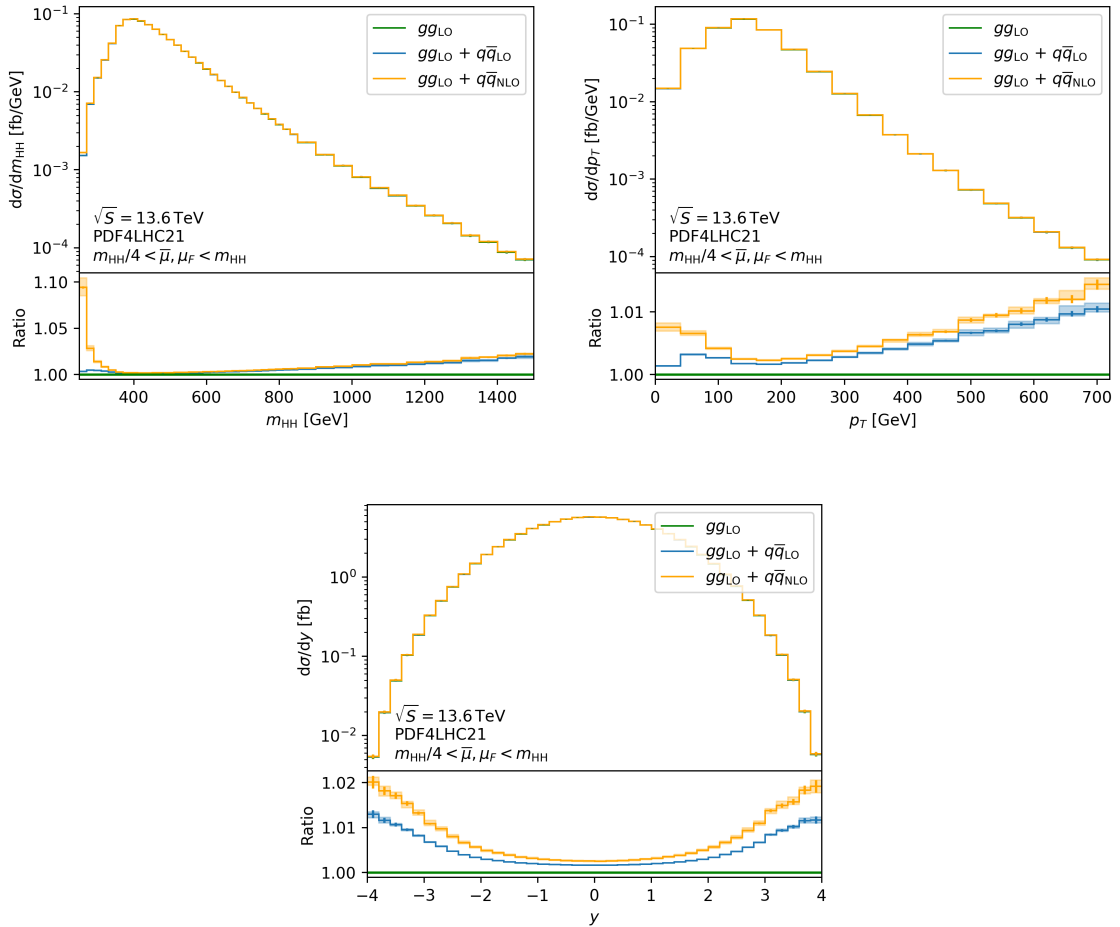


Figure 2: Invariant mass distribution of the Higgs pair (top left), transverse momentum distribution (top right) and rapidity distribution (bottom) of a single Higgs boson at a proton-proton centre-of-mass energy of $\sqrt{S} = 13.6$ TeV. The error bands represent the scale uncertainties of the quark-antiquark channel and the error bars indicate the statistical uncertainties from the Monte Carlo integration.

The rapidity distribution (bottom) is symmetric around $y = 0$ and nearly vanishes in the central bin, due to the $t \leftrightarrow u$ anti-symmetry of the LO and NLO virtual amplitudes.

The quark-antiquark channel, together with the NLO electroweak corrections to the gluon channel [79], will be included in the public library `ggHH` [13, 80] within the POWHEG-Box-V2 framework [39, 76, 77], making these results publicly available.

4.2 Bottom quark effects

We investigate the effect of initial-state massless bottom quarks by comparing the LO quark-antiquark channel with and without bottom quarks. Their inclusion allows for diagrams with internal top quarks, giving rise to new topologies, even when bottom quarks

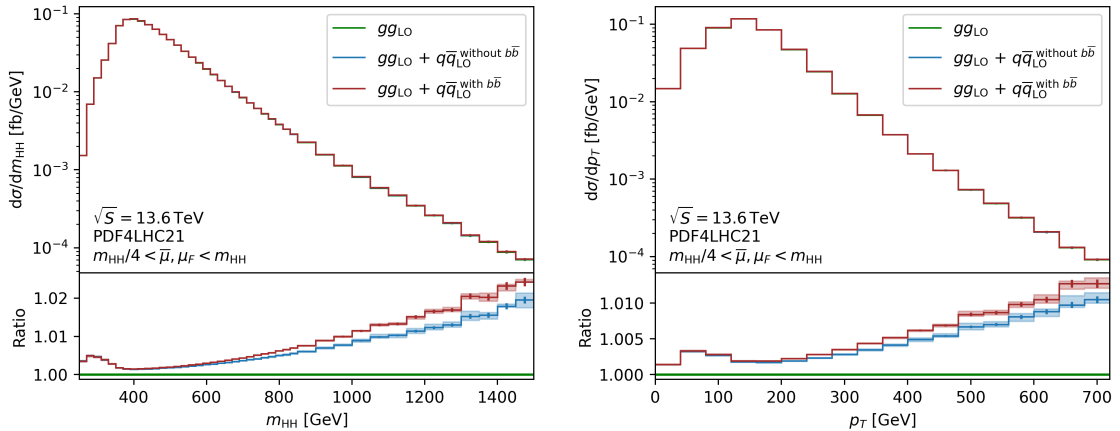


Figure 3: Effect of initial state bottom quarks on the invariant mass distribution of the Higgs boson pair (left) and transverse momentum distribution of a single Higgs boson (right). The error bands represent the scale uncertainties of the quark-antiquark channel while the error bars depict the statistical error.

are treated as massless. At LO, these contributions can be studied by including them into POWHEG-Box-V2 via GoSAM-3.0.

Figure 3 illustrates the impact of bottom quarks on the invariant mass distribution of the Higgs boson pair (left) and the transverse momentum distribution of a single Higgs boson (right). Including bottom quarks in the initial state leads to a maximum increase of 35% in the high-energy bins, compared to the LO quark-antiquark prediction without bottom quarks. At total cross section level, including (massless) bottom quarks in the initial state increases the quark-antiquark channel by about 10%, because the large- m_{HH} and large- p_T bins do not contribute much to the total cross section. We leave the investigation of the effects of massive bottom quarks in the gluon and quark-antiquark channels to future work, building on results of Ref. [81].

5 Conclusions

We have calculated the NLO QCD corrections to Higgs boson pair production in the quark-antiquark channel, where the Higgs boson pair at LO is produced through a loop containing electroweak bosons. Neglecting initial state b -quarks as their PDFs are suppressed, the NLO corrections involve two-loop amplitudes with four kinematical variables, including two mass scales, m_V and m_H , for which an analytic result has been achieved, using methods similar to the ones presented in Ref. [35]. The one-loop real radiation matrix elements have been generated with GoSAM-3.0 [51].

The results have been implemented into a Monte Carlo code based on the POWHEG-Box-V2 framework [39, 76, 77] to perform phenomenological studies. It turned out that the NLO corrections to the $q\bar{q}$ channel have a K-factor of about 1.6. The large K-factor

can be understood from contributions at low m_{HH} where a hard jet recoils against the Higgs boson pair, and also stems from the fact that the real radiation corrections open up new partonic channels: the qg channel, only present in the real corrections, profits from the large gluon luminosity at the LHC.

While these contributions still amount to less than 1% of the LO cross section in the gluon channel, the corrections are important at the differential level: they enhance the m_{HH} distribution close to the Higgs boson pair production threshold by almost 10% (with 20 GeV bins), and also show a Sudakov-type enhancement at high energies. As the low- m_{HH} region is very sensitive to modifications of the trilinear Higgs coupling, it is very important to control this region well, and therefore these contributions are not negligible in view of the high-quality data anticipated for the High-Luminosity LHC.

Having addressed the light-quark contributions, the next steps are a detailed study of massive bottom quark effects for Higgs boson pair production, and the combination of the results presented here with corrections of electroweak and QCD type in the gluon channel.

Acknowledgments

We would like to thank Jens Braun, Benjamin Campillo, Marius Höfer, Stephen Jones, Matthias Kerner, Pau Petit Rosàs, Chiara Signorile-Signorile and Augustin Vestner for useful discussions. M.B. wishes to thank Barbara Jäger for her support during the final stages of this project. This work is supported by the *Deutsche Forschungsgemeinschaft* (DFG, German Research Foundation) under grant no. 396021762 - TRR 257, and by the Leverhulme Trust, LIP-2021-014.

A Canonical DEQ for $\mathcal{A}^{(1)}$

In this appendix, we provide the canonical differential equations that obey the functions that contribute to $\mathcal{A}^{(1)}$,

$$d\vec{\omega}_{1;0} = d\Omega_{1;0} \vec{\omega}_{1;0}, \quad (A.1)$$

with,

$$\vec{w}_{3:0} = \{w_{10}^{(0)}, w_{11}^{(1)}, w_{21}^{(1)}, w_{51}^{(1)}, w_{71}^{(1)}, w_{22}^{(2)}, w_{72}^{(2)}, w_{102}^{(2)}, w_{132}^{(2)}, w_{202}^{(2)}, w_{232}^{(2)}\}, \quad (A.2)$$

the only non-vanishing boundary value at $s = 0$,

$$w_{10}^{(0)}|_{s=0} = -1, \quad (A.3)$$

and with the matrix of coefficients,

$$\Omega_{1;0} = \begin{pmatrix} 0 & 0 & 0 & 0 & 0 & 0 \dots 0 \\ -2L_{41} & 0 & 0 & 0 & 0 & 0 \dots 0 \\ -4L_{10} & 0 & 0 & 0 & 0 & 0 \dots 0 \\ 2L_{38} & 0 & 0 & 0 & 0 & 0 \dots 0 \\ -4L_{11} & 0 & 0 & 0 & 0 & 0 \dots 0 \\ 0 & -\frac{L_{39}}{4} - \frac{L_{41}}{8} & \frac{L_{21}}{4} - \frac{L_3}{4} & 0 & 0 & 0 \dots 0 \\ 0 & \frac{L_{54}}{4} & 0 & \frac{L_{52}}{4} & 0 & 0 \dots 0 \\ 0 & -\frac{L_{62}}{2} & -\frac{L_{37}}{2} & \frac{L_{61}}{4} & 0 & 0 \dots 0 \\ 0 & 0 & 0 & \frac{L_{38}}{4} & 0 & 0 \dots 0 \\ 0 & -\frac{L_{40}}{4} - \frac{L_{41}}{8} & 0 & 0 & \frac{L_{22}}{4} - \frac{L_4}{4} & 0 \dots 0 \\ 0 & -\frac{L_{70}}{2} & 0 & -\frac{L_{66}}{4} & -\frac{L_{49}}{2} & 0 \dots 0 \end{pmatrix}, \quad (\text{A.4})$$

where the integration kernels are,

$$\begin{aligned} L_3 &= \log(t), & L_{40} &= \log\left(\frac{m_H^2 - r_5 - 2u}{m_H^2 + r_5 - 2u}\right), \\ L_4 &= \log(u), & L_{41} &= \log\left(\frac{m_H^2 - r_5 - 2}{m_H^2 + r_5 - 2}\right), \\ L_{10} &= \log(1 - t), & L_{49} &= \log\left(\frac{s(1 - u) - r_8}{r_8 + s(1 - u)}\right), \\ L_{11} &= \log(1 - u), & L_{52} &= \log\left(\frac{s(2m_H^2 - s) - r_1 r_4}{s(2m_H^2 - s) + r_1 r_4}\right), \\ L_{21} &= \log((1 - t)m_H^2 + t^2), & L_{54} &= \log\left(\frac{(s + 8)m_H^2 - 2m_H^4 - r_1 r_5 - 2s}{(s + 8)m_H^2 - 2m_H^4 + r_1 r_5 - 2s}\right), \\ L_{22} &= \log((1 - u)m_H^2 + u^2), & L_{61} &= \log\left(\frac{-r_3 r_4 - s(st - 3t + u)}{r_3 r_4 - s(st - 3t + u)}\right), \\ L_{37} &= \log\left(\frac{s(1 - t) - r_3}{r_3 + s(1 - t)}\right), & L_{62} &= \log\left(\frac{s((1 - t)m_H^2 + 2t) - r_3 r_5}{s((1 - t)m_H^2 + 2t) + r_3 r_5}\right), \\ L_{38} &= \log\left(\frac{-r_4 - s + 2}{r_4 - s + 2}\right), & L_{66} &= \log\left(\frac{s(su + t - 3u) - r_4 r_8}{r_4 r_8 + s(su + t - 3u)}\right), \\ L_{39} &= \log\left(\frac{m_H^2 - r_5 - 2t}{m_H^2 + r_5 - 2t}\right), & L_{70} &= \log\left(\frac{s((1 - u)m_H^2 + 2u) - r_5 r_8}{s((1 - u)m_H^2 + 2u) + r_5 r_8}\right), \end{aligned} \quad (\text{A.5})$$

and square roots,

$$\begin{aligned} r_1 &= \sqrt{s(s - 4m_H^2)}, \\ r_3 &= \sqrt{s(m_V^4(s - 4m_H^2) + st^2 - 2m_V^2 t(t - u))}, \\ r_4 &= \sqrt{s(s - 4m_V^2)}, \\ r_5 &= \sqrt{m_H^2(m_H^2 - 4m_V^2)}, \\ r_8 &= \sqrt{s(m_V^4(s - 4m_H^2) + su^2 + 2m_V^2 u(t - u))}. \end{aligned} \quad (\text{A.6})$$

References

- [1] ATLAS, CMS collaboration, G. Aad et al., *Highlights of the HL-LHC physics projections by ATLAS and CMS*, [2504.00672](#).
- [2] O. J. P. Eboli, G. C. Marques, S. F. Novaes and A. A. Natale, *TWIN HIGGS BOSON PRODUCTION*, [Phys. Lett. B 197 \(1987\) 269–272](#).
- [3] E. W. N. Glover and J. J. van der Bij, *HIGGS BOSON PAIR PRODUCTION VIA GLUON FUSION*, [Nucl. Phys. B 309 \(1988\) 282–294](#).
- [4] S. Dawson, S. Dittmaier and M. Spira, *Neutral Higgs boson pair production at hadron colliders: QCD corrections*, [Phys. Rev. D 58 \(1998\) 115012](#), [[hep-ph/9805244](#)].
- [5] S. Borowka, N. Greiner, G. Heinrich, S. P. Jones, M. Kerner, J. Schlenk, U. Schubert and T. Zirke, *Higgs Boson Pair Production in Gluon Fusion at Next-to-Leading Order with Full Top-Quark Mass Dependence*, [Phys. Rev. Lett. 117 \(2016\) 012001](#), [[1604.06447](#)].
- [6] S. Borowka, N. Greiner, G. Heinrich, S. P. Jones, M. Kerner, J. Schlenk and T. Zirke, *Full top quark mass dependence in Higgs boson pair production at NLO*, [JHEP 10 \(2016\) 107](#), [[1608.04798](#)].
- [7] J. Baglio, F. Campanario, S. Glaus, M. Mühlleitner, M. Spira and J. Streicher, *Gluon fusion into Higgs pairs at NLO QCD and the top mass scheme*, [Eur. Phys. J. C 79 \(2019\) 459](#), [[1811.05692](#)].
- [8] J. Davies, G. Heinrich, S. P. Jones, M. Kerner, G. Mishima, M. Steinhauser and D. Wellmann, *Double Higgs boson production at NLO: combining the exact numerical result and high-energy expansion*, [JHEP 11 \(2019\) 024](#), [[1907.06408](#)].
- [9] J. Baglio, F. Campanario, S. Glaus, M. Mühlleitner, J. Ronca, M. Spira and J. Streicher, *Higgs-Pair Production via Gluon Fusion at Hadron Colliders: NLO QCD Corrections*, [JHEP 04 \(2020\) 181](#), [[2003.03227](#)].
- [10] M. Grazzini, G. Heinrich, S. Jones, S. Kallweit, M. Kerner, J. M. Lindert and J. Mazzitelli, *Higgs boson pair production at NNLO with top quark mass effects*, [JHEP 05 \(2018\) 059](#), [[1803.02463](#)].
- [11] D. de Florian, M. Grazzini, C. Hanga, S. Kallweit, J. M. Lindert, P. Maierhöfer, J. Mazzitelli and D. Rathlev, *Differential Higgs Boson Pair Production at Next-to-Next-to-Leading Order in QCD*, [JHEP 09 \(2016\) 151](#), [[1606.09519](#)].
- [12] J. Grigo, J. Hoff and M. Steinhauser, *Higgs boson pair production: top quark mass effects at NLO and NNLO*, [Nucl. Phys. B 900 \(2015\) 412–430](#), [[1508.00909](#)].
- [13] G. Heinrich, S. P. Jones, M. Kerner, G. Luisoni and E. Vryonidou, *NLO predictions for Higgs boson pair production with full top quark mass dependence matched to parton showers*, [JHEP 08 \(2017\) 088](#), [[1703.09252](#)].
- [14] S. Jones and S. Kuttimalai, *Parton Shower and NLO-Matching uncertainties in Higgs Boson Pair Production*, [JHEP 02 \(2018\) 176](#), [[1711.03319](#)].
- [15] G. Heinrich, S. P. Jones, M. Kerner, G. Luisoni and L. Scyboz, *Probing the trilinear Higgs boson coupling in di-Higgs production at NLO QCD including parton shower effects*, [JHEP 06 \(2019\) 066](#), [[1903.08137](#)].
- [16] E. Bagnaschi, G. Degrassi and R. Gröber, *Higgs boson pair production at NLO in the*

POWHEG approach and the top quark mass uncertainties, *Eur. Phys. J. C* **83** (2023) 1054, [[2309.10525](#)].

[17] J. Davies, K. Schönwald, M. Steinhauser and D. Stremmer, *ggry: A flexible library to compute gluon-induced cross sections*, *Comput. Phys. Commun.* **320** (2026) 109933, [[2506.04323](#)].

[18] S. Alioli, G. Marinelli and D. Napoletano, *NNLO+PS double Higgs boson production with top-quark mass corrections in GENEVA*, *JHEP* **09** (2025) 206, [[2507.08558](#)].

[19] L.-B. Chen, H. T. Li, H.-S. Shao and J. Wang, *Higgs boson pair production via gluon fusion at N^3LO in QCD*, *Phys. Lett. B* **803** (2020) 135292, [[1909.06808](#)].

[20] L.-B. Chen, H. T. Li, H.-S. Shao and J. Wang, *The gluon-fusion production of Higgs boson pair: N^3LO QCD corrections and top-quark mass effects*, *JHEP* **03** (2020) 072, [[1912.13001](#)].

[21] A. A H and H.-S. Shao, *N^3LO+N^3LL QCD improved Higgs pair cross sections*, *JHEP* **02** (2023) 067, [[2209.03914](#)].

[22] J. Baglio, F. Campanario, S. Glaus, M. Mühlleitner, J. Ronca and M. Spira, *$gg \rightarrow HH$: Combined uncertainties*, *Phys. Rev. D* **103** (2021) 056002, [[2008.11626](#)].

[23] S. Jaskiewicz, S. Jones, R. Szafron and Y. Ulrich, *The structure of quark mass corrections in the $gg \rightarrow HH$ amplitude at high-energy*, *JHEP* **09** (2025) 015, [[2501.00587](#)].

[24] J. Davies, K. Schönwald and M. Steinhauser, *Towards $gg \rightarrow HH$ at next-to-next-to-leading order: Light-fermionic three-loop corrections*, *Phys. Lett. B* **845** (2023) 138146, [[2307.04796](#)].

[25] J. Davies, K. Schönwald, M. Steinhauser and M. Vitti, *Three-loop corrections to Higgs boson pair production: reducible contribution*, *JHEP* **08** (2024) 096, [[2405.20372](#)].

[26] J. Davies, K. Schönwald and M. Steinhauser, *Three-loop large- N_c virtual corrections to $gg \rightarrow HH$ in the forward limit*, *JHEP* **08** (2025) 192, [[2503.17449](#)].

[27] Z. Hu and T. Liu, *Double logarithmic contribution to Higgs pair production in the high-energy limit*, [2509.06381](#).

[28] S. Borowka, C. Duhr, F. Maltoni, D. Pagani, A. Shivaji and X. Zhao, *Probing the scalar potential via double Higgs boson production at hadron colliders*, *JHEP* **04** (2019) 016, [[1811.12366](#)].

[29] M. Mühlleitner, J. Schlenk and M. Spira, *Top-Yukawa-induced corrections to Higgs pair production*, *JHEP* **10** (2022) 185, [[2207.02524](#)].

[30] J. Davies, G. Mishima, K. Schönwald, M. Steinhauser and H. Zhang, *Higgs boson contribution to the leading two-loop Yukawa corrections to $gg \rightarrow HH$* , *JHEP* **08** (2022) 259, [[2207.02587](#)].

[31] W. Bizoń, U. Haisch, L. Rottoli, Z. Gillis, B. Moser and P. Windischhofer, *Addendum to: Constraints on the quartic Higgs self-coupling from double-Higgs production at future hadron colliders* [*JHEP* 10 (2019) 267], *JHEP* **02** (2024) 170, [[2402.03463](#)].

[32] J.-L. Ding et al., *Constraining the Higgs potential using multi-Higgs production*, [2601.13248](#).

[33] G. Heinrich, S. Jones, M. Kerner, T. Stone and A. Vestner, *Electroweak corrections to Higgs boson pair production: the top-Yukawa and self-coupling contributions*, *JHEP* **11** (2024) 040, [[2407.04653](#)].

[34] J. Davies, K. Schönwald, M. Steinhauser and H. Zhang, *Analytic next-to-leading order Yukawa and Higgs boson self-coupling corrections to $gg \rightarrow HH$ at high energies*, *JHEP* **04** (2025) 193, [[2501.17920](#)].

[35] M. Bonetti, P. Rendler and W. J. Torres Bobadilla, *Two-loop light-quark Electroweak corrections to Higgs boson pair production in gluon fusion*, *JHEP* **07** (2025) 024, [[2503.16620](#)].

[36] A. Bhattacharya, F. Campanario, S. Carlotti, J. Chang, J. Mazzitelli, M. Mühlleitner, J. Ronca and M. Spira, *Higgs-Pair Production via Gluon Fusion: Top-Yukawa- and light-quark-induced electroweak Corrections*, [2512.14823](#).

[37] J. Davies, K. Schönwald, M. Steinhauser and H. Zhang, *Next-to-leading order electroweak corrections to $gg \rightarrow HH$ and $gg \rightarrow gH$ in the large- m_t limit*, *JHEP* **10** (2023) 033, [[2308.01355](#)].

[38] H.-Y. Bi, L.-H. Huang, R.-J. Huang, Y.-Q. Ma and H.-M. Yu, *Electroweak Corrections to Double Higgs Production at the LHC*, *Phys. Rev. Lett.* **132** (2024) 231802, [[2311.16963](#)].

[39] S. Alioli, P. Nason, C. Oleari and E. Re, *A general framework for implementing NLO calculations in shower Monte Carlo programs: the POWHEG BOX*, *JHEP* **06** (2010) 043, [[1002.2581](#)].

[40] D. Kreimer, *The $\gamma(5)$ Problem and Anomalies: A Clifford Algebra Approach*, *Phys. Lett. B* **237** (1990) 59–62.

[41] J. G. Korner, D. Kreimer and K. Schilcher, *A Practicable gamma(5) scheme in dimensional regularization*, *Z. Phys. C* **54** (1992) 503–512.

[42] J. C. Romao and J. P. Silva, *A resource for signs and Feynman diagrams of the Standard Model*, *Int. J. Mod. Phys. A* **27** (2012) 1230025, [[1209.6213](#)].

[43] A. Denner and S. Dittmaier, *Electroweak Radiative Corrections for Collider Physics*, *Phys. Rept.* **864** (2020) 1–163, [[1912.06823](#)].

[44] M. Bonetti, E. Panzer and L. Tancredi, *Two-loop mixed QCD-EW corrections to $q\bar{q} \rightarrow Hg$, $qg \rightarrow Hq$, and $\bar{q}g \rightarrow H\bar{q}$* , *JHEP* **06** (2022) 115, [[2203.17202](#)].

[45] T. Peraro and L. Tancredi, *Physical projectors for multi-leg helicity amplitudes*, *JHEP* **07** (2019) 114, [[1906.03298](#)].

[46] T. Peraro and L. Tancredi, *Tensor decomposition for bosonic and fermionic scattering amplitudes*, *Phys. Rev. D* **103** (2021) 054042, [[2012.00820](#)].

[47] S. Catani, *The Singular behavior of QCD amplitudes at two loop order*, *Phys. Lett. B* **427** (1998) 161–171, [[hep-ph/9802439](#)].

[48] S. Catani and M. Grazzini, *The soft gluon current at one loop order*, *Nucl. Phys. B* **591** (2000) 435–454, [[hep-ph/0007142](#)].

[49] G. Cullen, N. Greiner, G. Heinrich, G. Luisoni, P. Mastrolia, G. Ossola, T. Reiter and F. Tramontano, *Automated One-Loop Calculations with GoSam*, *Eur. Phys. J. C* **72** (2012) 1889, [[1111.2034](#)].

[50] G. Cullen, H. van Deurzen, N. Greiner, G. Heinrich, G. Luisoni, P. Mastrolia, E. Mirabella, G. Ossola, T. Peraro, J. Schlenk, J. von Soden-Fraunhofen and F. Tramontano, *GOSAM-2.0: a tool for automated one-loop calculations within the Standard Model and beyond*, *Eur. Phys. J. C* **74** (2014) 3001, [[1404.7096](#)].

[51] J. Braun, B. Campillo Aveleira, G. Heinrich, M. Höfer, S. P. Jones, M. Kerner, J. Lang and V. Magerya, *One-Loop Calculations in Effective Field Theories with GoSam-3.0*, *SciPost Phys. Codebases* (2026) **62**, [[2507.23549](#)].

[52] K. Chetyrkin and F. Tkachov, *Integration by Parts: The Algorithm to Calculate beta Functions in 4 Loops*, *Nucl.Phys. B* **192** (1981) 159–204.

[53] S. Laporta, *High-precision calculation of multiloop Feynman integrals by difference equations*, *Int. J. Mod. Phys. A* **15** (2000) 5087–5159, [[hep-ph/0102033](#)].

[54] R. Lewis, *Computer Algebra System Fermat*. <http://home.bway.net/lewis/>.

[55] A. von Manteuffel and C. Studerus, *Reduze 2 - Distributed Feynman Integral Reduction*, [1201.4330](#).

[56] P. Maierhöfer, J. Usovitsch and P. Uwer, *Kira—A Feynman integral reduction program*, *Comput. Phys. Commun.* **230** (2018) 99–112, [[1705.05610](#)].

[57] J. Klappert and F. Lange, *Reconstructing rational functions with FireFly*, *Comput. Phys. Commun.* **247** (2020) 106951, [[1904.00009](#)].

[58] J. Klappert, F. Lange, P. Maierhöfer and J. Usovitsch, *Integral reduction with Kira 2.0 and finite field methods*, *Comput. Phys. Commun.* **266** (2021) 108024, [[2008.06494](#)].

[59] J. Klappert, S. Y. Klein and F. Lange, *Interpolation of dense and sparse rational functions and other improvements in FireFly*, *Comput. Phys. Commun.* **264** (2021) 107968, [[2004.01463](#)].

[60] J. M. Henn, *Multiloop integrals in dimensional regularization made simple*, *Phys. Rev. Lett.* **110** (2013) 251601, [[1304.1806](#)].

[61] R. N. Lee, *Presenting LiteRed: a tool for the Loop InTEgrals REDuction*, [1212.2685](#).

[62] T. Peraro, *FiniteFlow: multivariate functional reconstruction using finite fields and dataflow graphs*, *JHEP* **07** (2019) 031, [[1905.08019](#)].

[63] W. Flieger and W. J. Torres Bobadilla, *Landau and leading singularities in arbitrary space-time dimensions*, *Eur. Phys. J. Plus* **139** (2024) 1022, [[2210.09872](#)].

[64] J. Henn, B. Mistlberger, V. A. Smirnov and P. Wasser, *Constructing d-log integrands and computing master integrals for three-loop four-particle scattering*, *JHEP* **04** (2020) 167, [[2002.09492](#)].

[65] D. Chicherin, V. Sotnikov and S. Zoia, *Pentagon functions for one-mass planar scattering amplitudes*, *JHEP* **01** (2022) 096, [[2110.10111](#)].

[66] T. Gehrmann, J. Henn, P. Jakubčík, J. Lim, C. C. Mella, N. Syrrakos, L. Tancredi and W. J. Torres Bobadilla, *Graded transcendental functions: an application to four-point amplitudes with one off-shell leg*, *JHEP* **12** (2024) 215, [[2410.19088](#)].

[67] M. Bonetti, G. Heinrich, P. Rendler and W. J. Torres Bobadilla, *Ancillary files for “NLO QCD corrections to the electroweak production of a Higgs boson pair in the quark-antiquark channel”*, Jan., 2026. [10.5281/zenodo.18285680](#).

[68] F. Moriello, *Generalised power series expansions for the elliptic planar families of Higgs + jet production at two loops*, *JHEP* **01** (2020) 150, [[1907.13234](#)].

[69] M. Hidding, *DiffExp, a Mathematica package for computing Feynman integrals in terms of one-dimensional series expansions*, *Comput. Phys. Commun.* **269** (2021) 108125, [[2006.05510](#)].

- [70] T. Armadillo, R. Bonciani, S. Devoto, N. Rana and A. Vicini, *Evaluation of Feynman integrals with arbitrary complex masses via series expansions*, *Comput. Phys. Commun.* **282** (2023) 108545, [[2205.03345](#)].
- [71] R. M. Prisco, J. Ronca and F. Tramontano, *LINE: Loop Integrals Numerical Evaluation*, *JHEP* **07** (2025) 219, [[2501.01943](#)].
- [72] P. Petit Rosàs and W. J. Torres Bobadilla, *Fast evaluation of Feynman integrals for Monte Carlo generators*, *JHEP* **09** (2025) 210, [[2507.12548](#)].
- [73] S. Caron-Huot and J. M. Henn, *Iterative structure of finite loop integrals*, *JHEP* **06** (2014) 114, [[1404.2922](#)].
- [74] X. Liu, Y.-Q. Ma and C.-Y. Wang, *A Systematic and Efficient Method to Compute Multi-loop Master Integrals*, *Phys. Lett. B* **779** (2018) 353–357, [[1711.09572](#)].
- [75] X. Liu and Y.-Q. Ma, *AMFlow: A Mathematica package for Feynman integrals computation via auxiliary mass flow*, *Comput. Phys. Commun.* **283** (2023) 108565, [[2201.11669](#)].
- [76] P. Nason, *A New method for combining NLO QCD with shower Monte Carlo algorithms*, *JHEP* **11** (2004) 040, [[hep-ph/0409146](#)].
- [77] S. Frixione, P. Nason and C. Oleari, *Matching NLO QCD computations with Parton Shower simulations: the POWHEG method*, *JHEP* **11** (2007) 070, [[0709.2092](#)].
- [78] PDF4LHC WORKING GROUP collaboration, R. D. Ball et al., *The PDF4LHC21 combination of global PDF fits for the LHC Run III*, *J. Phys. G* **49** (2022) 080501, [[2203.05506](#)].
- [79] M. Bonetti, G. Heinrich, S. Jones, M. Kerner, P. Rendler, T. Stone and A. Vestner, *NLO electroweak corrections to Higgs boson pair production*, *in preparation*, .
- [80] G. Heinrich, S. P. Jones, M. Kerner and L. Scyboz, *A non-linear EFT description of $gg \rightarrow HH$ at NLO interfaced to POWHEG*, *JHEP* **10** (2020) 021, [[2006.16877](#)].
- [81] D. Bürg, “Running coupling- and quark mass effects in Higgs boson pair production.” Bachelor Thesis, Karlsruhe Institute of Technology, 2023.